INTERNATIONAL JOURNAL FOR NUMERICAL METHODS IN FLUIDS, VOL. 24, 1271–1289 (1997)

FINITE ELEMENT SIMULATION OF VACUUM ARC REMELTING

D. K. GARTLING* AND P. A. SACKINGER

MS 08276, Engineering Sciences Center, Sandia National Laboratories, PO Box 5800, Albuquerque, NM 87185-0827, U.S.A.

SUMMARY

Vacuum arc remelting is a process for producing homogeneous ingots of reactive and macrosegregation-sensitive alloys. A mathematical model of the transport phenomena in the ingot melt is presented together with a discussion of the various simplifying assumptions and approximations that make the problem tractable, with particular attention on transport in the interdendritic mushy zone and on the magnetohydrodynamics. The finite element method is used to discretize the equations for the non-isothermal flow problem and the quasi-static electromagnetic problem. Coupling of the finite element solutions for the two field problems is accomplished using the Parallel Virtual Machine software. An analysis of the fluid flow and heat transport in the melt pool of the solidifying ingot shows some of the factors that influence ingot quality during quasi-steady growth conditions. Ⓒ1997 by John Wiley & Sons, Ltd.

Int. J. Numer. Meth. Fluids, **24**: 1271–1289, 1997

No. of Figures: 7. No. of Tables: 3. No. of References: 30.

KEY WORDS: viscous flow; solidification; electromagnetics; finite element

1. INTRODUCTION

Vacuum arc remelting (VAR) is a process for producing homogeneous ingots of reactive alloys that are prone to macrosegregation. The configuration of the VAR furnace is shown schematically in Figure 1. The process is designed to melt a consumable electrode in such a way as to produce a new ingot with better uniformity in metallurgical properties. A high current is passed through the electrode (cathode) and produces a metal vapour plasma arc between the electrode and the melt pool (anode) created in the water-cooled copper crucible. The plasma arc provides energy for melting the electrode, causing molten metal to drop into the melt pool. A key to the production of high-quality ingots is control of macrosegregation, which in turn implies control of the arc and the solidification process in the melt pool. As part of an effort towards understanding the many factors that contribute to the quality of VAR ingots, numerical techniques have been used to model the fluid flow, heat transfer and melt pool shape in VAR ingots as a function of various processing strategies.

The work in this area and other related areas involving molten metal processing has an extensive history, with the flow models becoming increasingly more sophisticated and complex. VAR-specific applications have been developed by Bertram and Zanner[1–3] and others,[4,5] mainly using finite difference/finite volume methods for the thermal or flow problem and simplified (analytic) field descriptions for the electromagnetic problem. More general alloy solidification studies using a variety of numerical methods are quite numerous and will not be catalogued here. Typical of this type of

*Correspondence to: D.K. Gartling, MS 08276, Engineering Sciences Center, Sandia National Laboratory, PO Box 5800, Albuquerque, NM 87185-0827, U.S.A.

CCC 0271–2091/97/121271–19 $17.50

Received 29 January 1996
Revised 19 April 1996

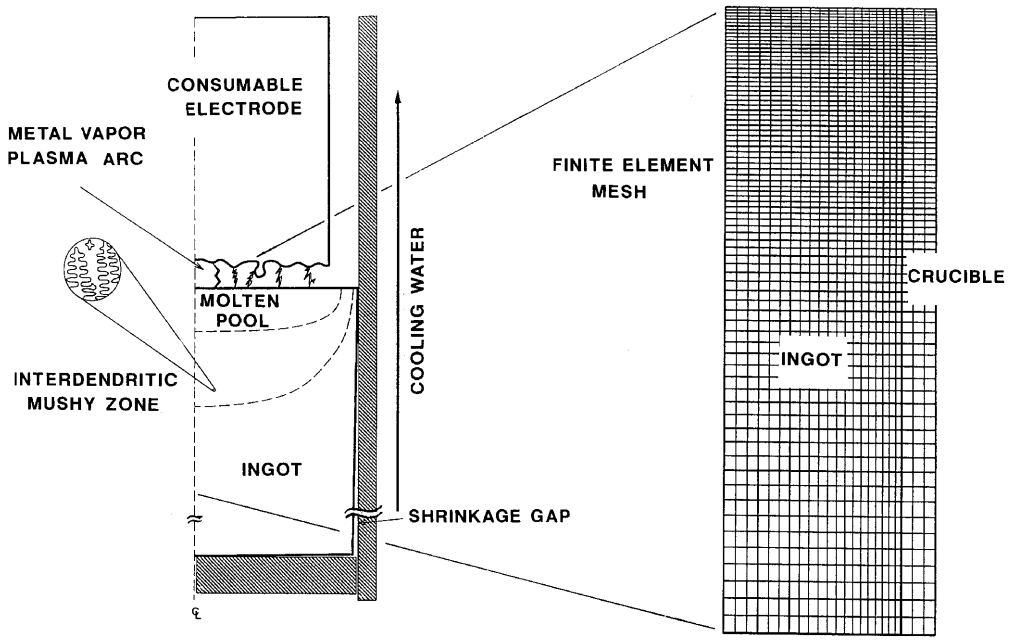

Figure 1. Schematic diagram of vacuum arc remelting (VAR) process and typical computational mesh. The metal vapour plasma arc provides heat to melt the cathode, which then drips into the ingot melt pool. Heat is extracted radially from the ingot through the water-cooled copper crucible

study is the work of Prescott and Incropera,[6,7] Voller and coworkers[8,9] and Beckermann and Viskanta[10] in developing mushy zone models for use in segregation simulations.

The objective of the present work was to develop a comprehensive and extensible computational model for the simulation of VAR processes. Because of the approach taken, the result of the work was somewhat more general and provides a broad capability to study many types of molten metal flows that are influenced by electromagnetic fields. Another by-product of the work was the development of a flexible method for coupling finite element codes for use in a variety of multiphysics applications. The coupling algorithm is outlined here but is covered in some detail in Reference 11.

The plan of the paper is as follows. In the next sections the mathematical statement of the VAR problem is given along with a few simplifying assumptions and approximations; the boundary conditions and material models are also reviewed. A brief section on non-dimensional forms is followed by a description of the numerical method and solution methods used on each field problem. A section on the coupling of the finite element codes precedes the discussion of several example situations. The paper concludes with comments on other applications and future directions for the proposed methodology.

2. MATHEMATICAL MODEL OF VAR

The first assumption in developing the VAR model is that the primary interest is in the ingot portion of the process (see Figure 1). Though the metal vapour arc is an important part of the overall process, the ability and need to model this region are limited. Therefore the domain for the computation will include only the ingot and perhaps the surrounding crucible. The need to include the crucible will depend on the ability to realistically condense the thermal and electromagnetic problems within the

crucible into boundary conditions for the ingot. A second assumption limits the spatial dependence of the fields to be purely axisymmetric; this assumption is justifiable owing to the cylindrical symmetry of the overall process, although small local deviations do occur. The numerical methods are developed as fully three-dimensional, since cases involving (imposed) time-dependent magnetic stirring in the circumferential directions are of interest as are situations with an eccentrically located electrode. The examples presented here are limited to the unstirred, two-dimensional case. Within the computational domain the physical processes of concern include the non-isothermal fluid mechanics of the melt pool, a region of non-isothermal flow in a porous medium that represents the interdendritic or mushy zone, solid body conduction through the solidified ingot and the distribution of the electric current (ohmic or Joule heating) and magnetic field (Lorentz force) throughout the domain. Each of these processes will be described separately.

2.1. Melt pool

The flow and transport in the ingot melt pool are described by the incompressible form of the Navier–Stokes equations and an accompanying energy equation. For this application the flow will be assumed laminar, though the occurrence of turbulence may eventually need to be considered. Also, interest in macrosegregation processes will require the inclusion of mass transport equations that are neglected for these first studies. Using vector notation, the required mass and momentum relations for the flow field are

$$\nabla \cdot \mathbf{u} = 0, \tag{1}$$

$$\rho_0 \left(\frac{\partial \mathbf{u}}{\partial t} + \mathbf{u} \cdot \nabla \mathbf{u} \right) = -\nabla P + \nabla \cdot (\mu \dot{\boldsymbol{\gamma}}) - \rho_0 \beta (T - T_0) \mathbf{g} + \mathbf{J} \times \mathbf{B}, \tag{2}$$

where the rate-of-strain tensor is defined as

$$\dot{\boldsymbol{\gamma}} = \nabla \mathbf{u} + (\nabla \mathbf{u})^{\mathrm{T}}$$

and $(\nabla \mathbf{u})^{\mathrm{T}}$ is the transpose of $\nabla \mathbf{u}$. Energy transport in the melt pool is described by

$$\rho_0 C_{\mathrm{p}} \left(\frac{\partial T}{\partial t} + \mathbf{u} \cdot \nabla T \right) = \nabla \cdot (k \nabla T) + \frac{1}{\sigma_{\mathrm{e}}} |\mathbf{J}|^2. \tag{3}$$

In writing (1)–(3), the Boussinesq approximation was invoked to allow density variations to only occur in the body force term. Also, the Lorentz force ($\mathbf{J} \times \mathbf{B}$) was included in the momentum equation and represents the body force due to the interaction of the electric current and magnetic field. The ohmic or Joule heating term $(|\mathbf{J}|^2/\sigma_{\mathrm{e}})$ was included in the energy equation as a volumetric source and represents the electromagnetic energy dissipated in the material. Note that the specific forms adopted for the Lorentz and Joule heating terms are consistent with the simplified Ohm's law[12] used in high-electrical-conductivity systems and defined in a subsequent section. The remaining parameters in the equations are defined as follows: $\mathbf{u}$ is the velocity vector, t is the time, ρ_0 is the reference density at the reference temperature T_0, P is the pressure, T is the temperature, μ is the viscosity, β is the coefficient of thermal expansion, C_{p} is the specific heat, k is the thermal conductivity, σ_{e} is the electric conductivity and $\mathbf{g}$ is the gravitational vector.

2.2. Mushy zone

The interdendritic region between the melt pool and the solidified ingot is modelled using a Brinkman–Darcy model for flow in a porous medium. This follows current theory and practice[6–10,13] in approximating the dendrite structure as an effective (anisotropic) porous layer with a permeability

that varies from zero at the solidus temperature to infinity at the liquidus temperature. The fluid motion in the porous layer is described by

$$\nabla \cdot \mathbf{u} = 0, \tag{4}$$

$$\frac{\rho_0}{\phi}\frac{\partial \mathbf{u}}{\partial t} + \frac{\rho_0}{\phi^2}\mathbf{u} \cdot \nabla \mathbf{u} = -\nabla P + \nabla \cdot (\mu_B \dot{\boldsymbol{\gamma}}) - \left(\frac{\mu}{\kappa}\right)\mathbf{u} - \rho_0 \beta (T - T_0)\mathbf{g} + \mathbf{J} \times \mathbf{B}. \tag{5}$$

If local thermal equilibrium between the interdendritic fluid and the porous matrix is assumed, then the effective energy equation for the porous region is

$$(\rho_0 C_p^e)\frac{\partial T}{\partial t} + (\rho_0 C_p^f)\mathbf{u} \cdot \nabla T = \nabla \cdot (k^e \nabla T) + \frac{1}{\sigma_e}|\mathbf{J}|^2. \tag{6}$$

In equations (4)–(6), $\mathbf{u}$ is the volume-averaged velocity vector (superficial or Darcy velocity), P is the volume-averaged pressure, ϕ is the porosity (liquid volume fraction) of the porous medium, κ is the permeability and μ_B is the Brinkman, or effective viscosity. The superscript 'e' indicates an effective property and the superscript 'f' denotes a fluid value; all other symbols retain their previous definitions. The effective properties (including the electric conductivity) are usually porosity-weighted averages of matrix and fluid properties. Equations (4)–(6) represent a significant generalization of the standard Darcy model for non-isothermal flow in a saturated porous medium. Note that the inclusion of the advective transport and stress terms in (5) permits the smooth transition from the flow in the melt pool to the flow in the mushy zone. This transition is controlled by the variation in material properties such as permeability which depend on the field variables such as temperature. The transition from the mushy zone to the solid ingot is also controlled by material property variations that asymptotically approach solid values as the porosity goes to zero. The problems and issues associated with coupling the above porous flow model with a viscous flow in an adjoining region (melt pool) were described and studied by Gartling *et al.*;[13] the methods developed there have been adopted for the present application.

2.3. Solidified ingot

After solidification the motion of the ingot becomes a simple solid body translation with a velocity defined by the global mass balance. The use of a Eulerian co-ordinate system implies that the advective part of the energy equation is still required. Thus the only equation needed for this region is (3) with a known velocity. As a practical matter with respect to numerical implementation, this region is actually treated as a fluid with a very large viscosity; equations (1)–(3) are used for this region. The large viscosity produces the required effect of solid body motion with the correct energy transport.

2.4. Electromagnetic fields

The relevant electromagnetic problem in the ingot is described by a quasi-static form of Maxwell's equations.[12,14,15] In rational MKSA notation these equations may be written for a conductive material as

$$\nabla \times \mathbf{E} = -\frac{\partial \mathbf{B}}{\partial t}, \tag{7}$$

$$\nabla \times \mathbf{H} = \mathbf{J}, \tag{8}$$

$$\nabla \cdot \mathbf{B} = 0, \tag{9}$$

where the vector field variables are the electric field intensity **E**, the magnetic field intensity **H**, the magnetic flux density **B** and the conduction current density **J**. A continuity condition on the current density is also defined by

$$\nabla \cdot \mathbf{J} = 0. \tag{10}$$

To complete the formulation, the constitutive relations for the material are required. The fluxes are related to the field variables by

$$\mathbf{B} = \mu_0 \mu_r \mathbf{H} = \mu_m \mathbf{H} \quad \text{or} \quad \mathbf{H} = \nu_0 \nu_r \mathbf{B} = \nu_m \mathbf{B}, \tag{11}$$

$$\mathbf{J} = \sigma_e \mathbf{E} \tag{12}$$

where μ_m is the magnetic permeability, ν_m is the magnetic reluctivity and σ_e is the electric conductivity. In equations (11) and (12) the subscripts 'r' and '0' on the material coefficients represent relative and base (or free space) values respectively. Note also that in general the material properties are tensorial in nature and may be field-dependent and anisotropic; some property relations may also exhibit hysteresis effects. Ohm's law (12) has been written in a simplified form[12] which neglects electric currents due to the motion of the conductive material. This is a good approximation for the high conductivity and low fluid velocities found in VAR. The above equations have also been written for the case of small magnetic Reynolds number,[12,14] which is defined as $Re_m = UL\sigma_e\mu_m$, where U is a typical fluid velocity and L is a representative length scale for the flow domain. The magnetic Reynolds number represents a ratio of magnetic convection to magnetic diffusion and for small values of Re_m the convective transport of the magnetic field may be neglected. For VAR a typical magnetic Reynolds number is $Re_m \approx 0{\cdot}04$ and convection of the **B**-field may be neglected; this approximation decouples the magnetic field from the fluid velocity field.

For use in numerical computation it is usual to rewrite the above system in terms of potential functions and thereby reduce the number of equations that must be solved. From equation (9) it follows that **B** is derivable from a vector potential[14] and thus

$$\mathbf{B} = \nabla \times \mathbf{A}, \tag{13}$$

where **A** is the magnetic vector potential. In addition, from equation (7) it can be shown that[14]

$$\mathbf{E} = -\nabla V - \frac{\partial \mathbf{A}}{\partial t}, \tag{14}$$

where V is the electric scalar potential. Using these two definitions and the relevant constitutive relations, equations (8) and (10) become

$$\nabla \times (\nu_m \nabla \times \mathbf{A}) = \mathbf{J} = \sigma_e \mathbf{E} = -\sigma_e \nabla V - \sigma_e \frac{\partial \mathbf{A}}{\partial t}, \tag{15}$$

$$\nabla \cdot \left(-\sigma_e \nabla V - \sigma_e \frac{\partial \mathbf{A}}{\partial t} \right) = 0. \tag{16}$$

These two equations provide the needed description for the electric and magnetic fields in the VAR problem and other magnetically driven flows. For the nominally time-independent DC currents found in VAR the time derivatives in (15) and (16) are eliminated and the equations may be solved in sequence with the electric potential equation (16) considered first. With known values of V the current densities in the region may be found from (14) and (12). Using the current density as a known source, equation (15) may then be solved for the magnetic potential and subsequently for the magnetic flux **B**. However, the ultimate quantities of interest are the Joule heating and Lorentz forces defined in (2) and (3). The electric and magnetic fields are present throughout the ingot and the

electric conductivity and magnetic permeability are necessarily functions of the material state (i.e. solid or liquid) and temperature. This dependence leads to the two-way coupling of the field problems and provides one of the major difficulties for this type of simulation.

For other applications with time-harmonic electromagnetic fields, such as electroslag melting and inductive melting, a phasor representation of the field variables is appropriate. This leads to a simplification of the time derivative terms in (15) and (16) but adds the difficulty of complex coefficients and variables within the equations.[15] Also, in some situations an additional gauge constraint such as $\nabla \cdot \mathbf{A} = 0$ must be placed on equations (15) and (16). This ensures the uniqueness of $\mathbf{A}$, since the unconstrained formulation only ensures that $\nabla \times \mathbf{A}$ is unique. This constraint is not required in the present case because the derived quantities of interest, namely the Lorentz force and Joule heating, depend only on the curl of the potential.

2.5. Material models

Alloy solidification is a complex process and the material models used in the numerical algorithm are critical to realistic and accurate simulations. In some cases accurate property information is not available (e.g. molten metal data) owing to measurement difficulties. Assumptions and limitations for the VAR property descriptions are outlined here.

The density of the material is assumed constant throughout the domain and all variations in density due to solidification are neglected. The latent heat of fusion is accounted for via an enthalpy method,[16] where the specific heat is a temperature-dependent function given by

$$C_p(T) = \begin{cases} C_p^s, & T < T_{sol}, \\ C_p^e + \Delta H_f^0/(T_{liq} - T_{sol}), & T_{sol} < T < T_{liq}, \\ C_p^f, & T_{liq} < T, \end{cases} \tag{17}$$

where T_{liq} and T_{sol} are the liquidus and solidus temperatures. The enthalpy released during solidification, ΔH_f^0, is approximated by assuming it to be a uniformly distributed over the temperature range of solidification, $T_{liq} - T_{sol}$. The base values of specific heat, C_p^f, C_p^s and C_p^e, correspond to fluid, solid and effective values respectively. Each base value may be an independent function of temperature, if required, and the effective value for the mushy zone is determined from the mixture rule $C_p^e = \phi C_p^f + (1 - \phi) C_p^s$, where ϕ is the local porosity or liquid volume fraction.

The thermal conductivity is temperature-dependent in both the solid and the fluid; the effective or mushy zone value is a porosity-weighted function similar to the form shown for the specific heat. The thermal expansion coefficient may be temperature-dependent within the fluid and mushy zone but is set to zero at the solidus temperature. The electric and magnetic properties σ_e and ν_m are generally temperature-dependent in both the fluid and solid regions when such data are available. The mushy zone again uses a porosity-weighted value for both electric conductivity and magnetic reluctivity.

Two viscosities have been defined in the basic equations, the standard fluid viscosity and the Brinkman viscosity for the porous layer. Owing to the absence of any experimental data and recognizing that the Brinkman viscosity must approach the fluid viscosity at the edge of the melt pool, the two viscosities have been set equal in the present model. The viscosity is taken to be a strong function of temperature (either linear or exponential) between the liquidus and solidus temperatures. At the solidus temperature the viscosity is typically set at a value 10^5–10^{10} times the liquidus value, effectively immobilizing the 'fluid'. Other viscosity models that depend on the local porosity[17] could also be used but have not yet been investigated. In concert with the change in viscosity across the mushy zone a variation in porous layer permeability and porosity is evaluated. The permeability for a dendrite layer is anisotropic with the principal directions for the tensor

oriented normal and tangent to the local isotherm, assuming steady solidification. Following Poirier,[18] the principal components of the permeability tensor may be described by

$$\kappa_n = \frac{m_n \phi^3}{(1-\phi)^2}, \qquad \kappa_t = \frac{m_t \phi^3}{(1-\phi)^{3/4}}, \tag{18}$$

where m_n and m_t are morphology coefficients that depend on the dendrite structure, that is. the primary and secondary dendrite arm spacings. The subscripts 'n' and 't' refer to directions normal and tangent to an isotherm. Equation (18) is similar to the standard Carmen–Kozeny relation for permeability as a function of porosity in general porous materials. The remaining relationship needed to close the material models is the dependence of porosity on temperature. Several possibilities exist, including a simple linear relation or the more complex Scheil equation[19] and related treatments that account for solute redistribution. To be consistent with the latent heat release, the present model employs the simplified linear relation

$$\phi = \frac{T - T_{sol}}{T_{liq} - T_{sol}}. \tag{19}$$

2.6. Boundary conditions

The boundary conditions adopted for the VAR model connect the computational region to the parts of the physical process that have been removed from consideration. A number of assumptions accompany these conditions, as will be explained in the following.

Referring to Figure 2, the upper boundary of the ingot is a free surface across which mass and energy are transported via intermittent droplets coming from random locations beneath the electrode. The fluid inflow boundary condition is set by the average specified melt rate, though the actual inflow distribution is not known. Under a quasi-steady melting assumption the inflow is distributed uniformly over the top of the ingot. This assumed spatial distribution is not viewed as critical, since the inflow velocity is small ($\sim 10^{-5}$ m s^{-1}) compared with the motion within the melt pool ($\sim 10^{-2}$ m s^{-1}). The upper surface is also assumed to be shear-free, which neglects Marangoni forces due to surface tension gradients caused by temperature and/or solute variations on the surface. Data on surface tension at elevated temperatures are sparse; this effect could be easily included for a flat free surface and with somewhat more difficulty for a deformed free boundary. Along the crucible boundary the fluid/solid moves with a vertical velocity given by the melt rate. At outflow the flow condition is a constant normal traction and zero radial velocity. These conditions are somewhat artificial, in the sense that the growth of a VAR ingot is inherently a time-dependent batch process. The top boundary of the ingot moves upwards as a slowly increasing function of time and the bottom boundary position remains fixed at the baseplate. However, from a numerical modelling perspective it is more convenient to invoke the quasi-steady approximation on a Eulerian grid and allow the ingot to move through the domain. This approximation is reasonable for the latter stages of ingot growth, when the ingot length has reached several ingot diameters and the growth rate has been held constant for several thermal diffusion times based on ingot radius. This approach is similar to the process of continuous casting.

Thermal boundary conditions for the ingot, which are illustrated in Figure 3, are the most difficult and involve the most approximation. Over the top surface of the ingot the net heat flux is specified with an assumed radial distribution. The assumed profile is a constant flux from the centreline of the ingot to a radius that is equal to the electrode radius; the flux decreases linearly from the edge of the electrode to the crucible wall. Energy is input to the melt pool surface from the plasma via several mechanisms, the most important being the advective flux of heat contained in the superheated molten

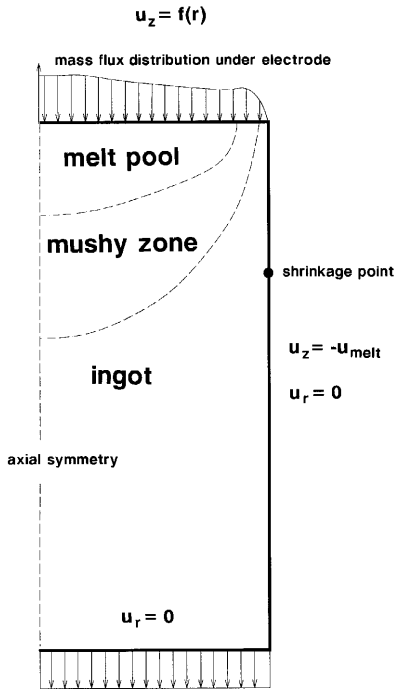

Figure 2. Flow boundary conditions for VAR. Molten metal droplets from the electrode fall into the melt pool, providing a temporally and spatically averaged inflow. Solidified material along the ingot–crucible boundary and at the bottom translates with the velocity given by the melt rate

metal droplets falling from the electrode and the heat flux due to electrons from the plasma striking the melt pool surface. Overall energy budgets for the process have been performed[2] using information from the input electrical power and the heat carried away by the cooling water. These global energy balances suggest that 50%–90% of the electrical power enters the melt pool surface in one form or another, with the exact amount depending on the material being melted, the size of the ingot and the operating conditions. In the present model the net heat flux boundary condition is partitioned into two components. A convective condition is used to represent the energy due to the droplet inflow and a specified flux accounts for the energy from the plasma. One of the major unknowns in this model is the plasma flux, though its magnitude can be bounded. These two effects were separated to aid in the control of the solution process.

As the ingot solidifies, it shrinks in diameter and eventually separates from the crucible, leaving a shrinkage gap that may or may not be filled with an inert gas. The thermal resistance along the ingot-crucible interface is therefore quite variable and is simulated with a heat transfer coefficient that varies with temperature and axial location. Above the separation point the contact between ingot and crucible is assumed to be very good and the heat transfer coefficient is quite high. Below separation the heat transfer coefficient is based on conduction through a gas layer, if it exists, and radiation between concentric cylinders. The point of separation is set by specifying the temperature T_{shrink} at which shrinkage occurs; the transition from one heat transfer coefficient to another occurs over a temperature interval centred on T_{shrink}. The shrink temperature is usually set well below the solidus temperature, though a reliable value for this parameter is not known. Consideration of the solid mechanics response of the ingot could eliminate the need for this type of parametrization. The

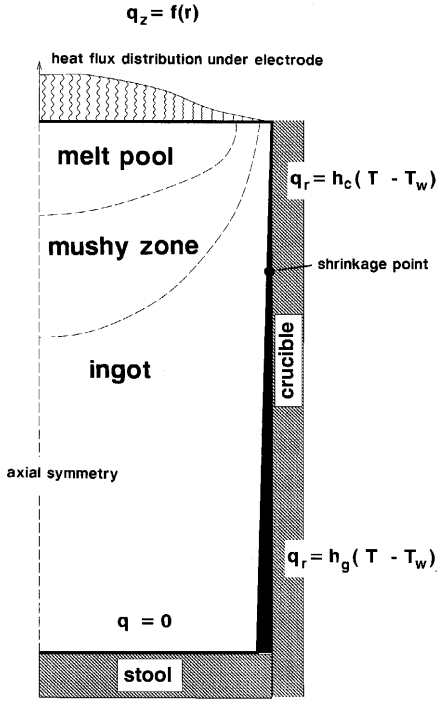

Figure 3. Thermal boundary conditions for VAR. Heat is input from the metal vapour arc and the superheated molten metal droplets from the electrode. The ingot–crucible heat transfer coefficient is high where contact is good and is low after the ingot separates from the crucible

thermal boundary condition at the bottom of the computational domain is the usual outflow condition of a zero conductive heat flux; the convective flux is left unconstrained.

The real electromagnetic environment during a VAR process is quite complex but can be simplified considerably for the purpose of modelling the fluid flow and heat transfer in the melt pool. The average current signal is DC, but superimposed upon this basic DC signal are fluctuations governed by the dynamics of the plasma, the cathode spots and the occasional drop shortening events during low-current melting. These phenomena all contribute to a current flux distribution on the ingot melt pool surface that varies in time and space. Fortunately, it is only the average temporal behaviour of the current that needs to be taken into account; the details of the electrical signature that occur on time scales faster than the time scales for thermal and momentum transport in the melt pool can be averaged to a good approximation.

The electric and magnetic boundary conditions are sketched in Figure 4. On the top surface of the ingot melt pool the electric current distribution is assumed to be of the form

$$J_z(r) = \sigma_e \nabla V = \frac{I_p}{2\pi R^2} j_0^1 \frac{J_0(j_0^1 r/R)}{J_1(j_0 1)}, \tag{20}$$

where I_p is the input current, R is the radius of the ingot, J_0 and J_1 are Bessel functions and j_0^1 is the first root of the Bessel function J_0. This distribution is physically reasonable and provides the simplest analytic solution to Laplace's equation (Ohm's law) on the cylindrical (ingot) domain.[20] Though the distribution in (20) corresponds to a simplified problem (no property variation and constant sidewall boundary conditions), it does provide a useful electrical boundary condition for the

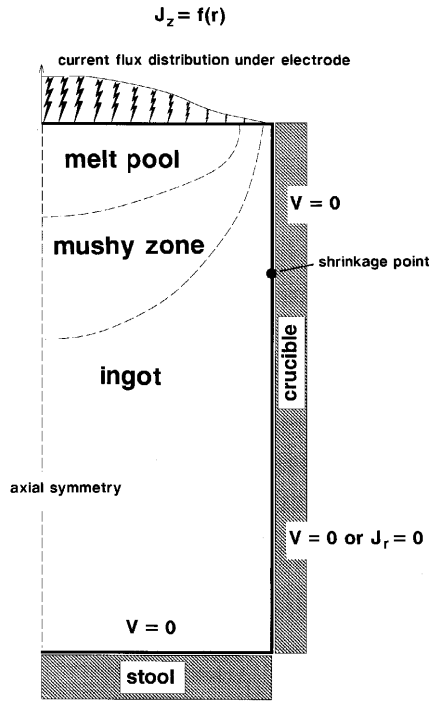

Figure 4. Electrical boundary conditions for VAR. The current flux distribution at the melt pool surface is specified. The ingot–crucible boundary is grounded where contact is good and is insulated after the ingot separates from the crucible. The bottom of the ingot is grounded

numerical simulation. The analytic solution for the case of a grounded sidewall and bottom also provides a check for the electromagnetic portion of the numerical algorith. Though the overall current for the VAR process is known, the fraction of the current that actually passes through the ingot is somewhat uncertain and is a function of the operating conditions. The parameter I_p is specified for the present model but could be removed as a variable with a more complete electromagnetic simulation that included the electrode, arc and losses to the crucible wall above the ingot.

The electrical boundary conditions on the sidewall and on the bottom of the computational domain are initially taken to be $V = 0$. The grounded bottom boundary condition for the ingot is reasonable, since electrical contact is generally good at the copper stool plate. However, this boundary condition is approximate, because the bottom of the computational domain does not coincide with the location of the stool. On the ingot–crucible boundary, above the shrinkage separation point, good electrical contact is expected and the grounded boundary condition is appropriate. Below the separation point an electrically insulated condition $\partial V/\partial n = 0$ is more appropriate and is used in some simulations. Note that even with a ground-type boundary along the entire sidewall more than 90% of the current passes to the crucible sidewall in the top ingot diameter and the current flux to the crucible in the shrinkage gap region is small. There is a significant difference between these two boundary conditions only when the separation point is close to the top of the ingot. The location of the separation point and the change in boundary condition are part of the data supplied to the electromagnetics code from the flow analysis. The magnetic boundary conditions are set on the radial and axial components of the magnetic potential; only the axial and radial components of **A** exist when the current is confined to the (r, z) plane and the geometry is axisymmetric. The radial component of

A is zero on the top and bottom of the ingot and the axial component is zero on the outside boundary of the ingot. The axial component on the top and bottom surfaces and the radial component on the outside boundary were left unconstrained, with natural boundary conditions being implied. These are approximations for an unbounded magnetic flux problem[14] and are reasonable as passive boundary conditions for the ingot.

2.7. Non-dimensional equations

Natural convection problems driven by a combination of thermal buoyancy and Lorentz forces are difficult to simulate numerically because of the large but opposing values of the force contributions. The presence of a melt zone also complicates the solution process, especially when a steady flow solution algorithm is used. It is often advantageous to non-dimensionalize the field equations and use the critical non-dimensional parameters to help in the control of the solution process.

In the present work the transport equations for the melt pool (1)–(6) were non-dimensionalized to produce the system

$$\nabla \cdot \mathbf{u}^* = 0, \tag{21}$$

$$\frac{\partial \mathbf{u}^*}{\partial^*} + \mathbf{u}^* \cdot \nabla \mathbf{u}^* = -\nabla P^* + \frac{1}{\sqrt{(Gr_0)}} \nabla \cdot (\mu^* \dot{\boldsymbol{\gamma}}^*) - \frac{1}{\sqrt{(Gr_0) Da_0}} \left(\frac{\mu^*}{\kappa^*} \right) \mathbf{u}^* - \beta^* \Theta^* + \frac{Ha_0^2}{Gr_0 Pr_{\mathrm{m}}} \mathbf{J}^* \times \mathbf{B}^*, \tag{22}$$

$$C_{\mathrm{p}}^* \left(\frac{\partial \Theta^*}{\partial^*} + \mathbf{u}^* \cdot \nabla \Theta^* \right) = \frac{1}{\sqrt{(Gr_0) Pr_0}} \nabla \cdot (k^* \nabla \Theta^*) + \frac{Jo_0}{\sqrt{(Gr_0) Pr_0}} |\mathbf{J}^*|^2, \tag{23}$$

where the superscript '*' now indicates a non-dimensional variable or function and the ∇ is also non-dimensional. The melt pool and mushy zone equations have been combined to produce (21)–(23), with the material property functions now defined such that they are valid throughout both regions. To arrive at (21)–(23), the primary variables were scaled according to

$$\begin{aligned} \mathbf{x}^* &= \mathbf{x}^*/R, \qquad \mathbf{u}^* = \mathbf{u}/U, \qquad t^* = tU/R, \\ \Theta^* &= (T - T_0)/\Delta T, \qquad \mathbf{J}^* = \mathbf{J}/J_0, \qquad \mathbf{B}^* = \mathbf{B}/B_0, \end{aligned} \tag{24}$$

where R is the ingot radius, the velocity scale $U = \sqrt{(g\beta_0 \Delta T R)}$ is a buoyancy velocity and the temperature scale is $\Delta T = T_{\mathrm{liq}} - T_{\mathrm{sol}}$, with a reference temperature $T_0 = \frac{1}{2}(T_{\mathrm{liq}} + T_{\mathrm{sol}})$. The variable material properties are normalized by reference values evaluated at T_0. The electromagnetic variables are scaled by $B_0 = \mu_{\mathrm{m}} J_0 R$ and $J_0 = I_{\mathrm{total}}/\pi R^2$, where I_{total} is the total input current to the ingot.

The non-dimensional parameters that occur in (21)–(23) are defined as the Prandtl number $Pr_0 = \mu_0 C_{\mathrm{p}_0}/k_0$, the Grashof number $Gr_0 = \rho^2 g \beta_0 \Delta T R^3/\mu_0^2$, the Darcy number $Da_0 = \kappa_0/R^2$, a magnetic Prandtl number $Pr_{\mathrm{m}} = \rho_0 \mu_{\mathrm{m}} \sigma_{\mathrm{e}}/\mu_0$, the Hartman number $Ha_0^2 = B_0^2 R^2 \sigma_{\mathrm{e}}/\mu_0$ and a Joule heating number $Jo_0 = J_0^2 R^2/\sigma_{\mathrm{e}} k_0 \Delta T$. Once the ingot material is selected, nominal values for several of these parameters can be determined. The remaining parameters such as Ha_0^2 and Jo_0 depend on the processing conditions. Representative values for the non-dimensional parameters will be given during the discussion of the ingot simulations. The Grashof and Hartman numbers were identified as the primary control parameters for the simulation since they provide the relative influence of the buoyancy and Lorentz forces. These parameters were used to assist in incrementally advancing the solution process to the desired, time-independent, flow state.

Boundary conditions for the non-isothermal flow problem were also made non-dimensional with the scalings listed in (24). The specified inflow velocity becomes $u_{\mathrm{in}}^* = u_{\mathrm{in}}/U = Pe/\sqrt{(Gr_0) Pr_0}$,

where the Peclet number is $u_{\text{in}}L/\alpha_0$ and α_0 is the thermal diffusivity. The heat flux over the top of the ingot transforms to a Biot number distribution $q_z^*(r^*) = Bi_z(r^*) = q_{in}(r)R/k_0\Delta T$ where q_{in} is the heat flux due to the plasma. The convective flux over the top of the ingot can be written as $q_z^*(r^*) = Bi_z(r^*)(\Theta^* - \Theta_l^*)$, where $Bi_z = h_z(r)R/k_0$, Θ_l^* is the liquidus temperature and h_z depends on the melt rate. The heat transfer along the ingot–crucible boundary was scaled in a similar manner to produce $q_r^*(z^*) = Bi_r(z^*)(\Theta^* - \Theta_w^*)$, with $Bi_r = h_r(z)R/k_0$. Θ_w^* is the cooling water temperature.

The electromagnetic equations could also have been reduced to a non-dimensional form. However, there was no apparent advantage in this type of scaling, since the equations were linear and could be solved without iteration. The important effects from the electromagnetics come from the derived variables and these were scaled after they had been communicated to the flow code.

3. NUMERICAL METHOD

The coupled fluid mechanics and electromagnetic problem outlined in the previous sections was converted to a discrete computational form through the use of a Galerkin-based method of weighted residuals (MWR) and a finite element approximation. Because the flow and electromagnetic solution schemes were developed separately, they will be described individually.

3.1. Incompressibility flow algorithm

The numerical solution to the non-isothermal flow problem in the ingot was carried out using the code NACHOS II,[21] which is based on a mixed finite element method. The formulation uses the primitive variable form of the equations as shown in (1)–(3) and includes the capability of transition to the Darcy–Brinkman equations given in (4)–(6). The development of the finite element equations corresponding to (1)–(6) is adequately treated elsewhere[13,21–23] and will only be summarized here.

The finite element equations resulting from the Galerkin MWR can be written in matrix form as

$$-\mathbf{Q}^{\mathrm{T}}\mathbf{U} = \mathbf{0}, \tag{25}$$

$$\mathbf{M}\dot{\mathbf{U}} + \mathbf{C}\mathbf{U} + \mathbf{A}\mathbf{U} - \mathbf{Q}\mathbf{P} + \mathbf{K}\mathbf{U} + \mathbf{B}\mathbf{T} = \mathbf{F}, \tag{26}$$

$$\mathbf{N}\dot{\mathbf{T}} + \mathbf{D}\mathbf{T} + \mathbf{L}\mathbf{T} = \mathbf{G}. \tag{27}$$

The vectors **U**, **P** and **T** represent the discrete (nodal) velocity, pressure and temperature fields. The matrices are the discrete forms of the terms shown in (1)–(6), with **M** and **N** being the mass and capacitance matrices, **C** and **D** the advection terms, **K** and **L** the diffusion operators, **A** the Darcy term, **Q** and $\mathbf{Q}^{\mathrm{T}}$ the gradient and divergence operators and **B** the body force term. The vectors **F** and **G** represent the surface stresses, applied fluxes and volumetric sources for the domain, including the Joule heating and Lorentz forces from the electromagnetic fields.

The element-level interpolation functions used in the present work consisted of quadratic Lagrange functions for the velocity and temperature and linear discontinuous pressure approximations. Time-dependent problems are solved using an implicit predictor–corrector (Adams–Bashforth, trapezoid rule) algorithm with adaptive time step control. Time-independent solutions were solved with a Picard or Newton iteration method; zeroth-order continuation was used to reach solutions with significant convection. All the solution methods solved the equations in a fully coupled manner and used a direct solver for the resulting linear algebra problem.

3.2. Electromagnetic algorithm

The electromagnetic fields for the VAR problem were computed using the TORO II code,[24] which is based on the electric scalar and magnetic vector potential form of Mawell's equations. The code was designed to simulate a variety of electromagnetic problems, including electrostatics, steady current flows and eddy currents. The quasi-steady VAR application is a magnetostatic problem that is described by a reduced form of (15) and (16). That is,

$$\nabla \times (\nu_m \nabla \times \mathbf{A}) = \mathbf{J} = -\sigma_e \nabla V, \tag{28}$$

$$-\nabla \cdot (\sigma_e \nabla V) = 0. \tag{29}$$

The finite element equations resulting from the Galerkin MWR used on (28) and (29) can be written in matrix form as

$$\tilde{\mathbf{K}}\mathbf{A} = \tilde{\mathbf{G}} + \tilde{\mathbf{G}}_{\mathbf{J}}, \tag{30}$$

$$\tilde{\mathbf{L}}\mathbf{V} = \tilde{\mathbf{F}}. \tag{31}$$

In equations (30) and (31) the vectors **V** and **A** represent the nodal values of the electric potential and the components of the magnetic vector potential; two components, A_r and A_z, exist for the VAR problem. The operator $\tilde{\mathbf{L}}$ is the weak form of the Laplacian and **K** is the weak form of the double curl operator. The vectors **F** and **G** contain boundary conditions for the current flow and magnetic flux; the vector $\mathbf{G}_{\mathbf{J}}$ represents the current sources derived from the gradient of the electric potential.

Equations (30) and (31) are decoupled and, as noted previously, may be solved sequentially, with the electric field being processed first. For VAR applications the equations are linear, though the material properties contained in **L** and **K** are temperature-dependent. Solution of the linear matrix problems associated with (30) and (31) was accomplished with a preconditioned conjugate gradient iterative method. The element-level interpolative functions used in the present work consisted of quadratic Lagrange functions for the potentials. The Joule heating and Lorentz forces needed in the flow simulation are computed from derivatives of the potentials evaluated at the integration points of each element.

3.3. Coupling algorithm

As is evident from the VAR problem, there is often a need to couple two or more solution processes (computer codes) in order to simulate a complex multiphysics problem. In many previous cases this type of requirement has led to the development of a fully integrated code that contained all the necessary mechanics for a specific application. This approach is time-consuming and expensive, with the end product often lacking the flexibility or generality for other applications. It is generally very difficult to anticipate the extent and types of coupling that may occur in a wide variety of mechanics applications.

The solution arrived at for the VAR problem is quite general and makes use of well-developed software libraries. In essence the codes are coupled using a data exchange method under a master/slave paradigm. In the VAR example the flow solution is the master process, since the flow dictates the major time and length scales for the simulation; the electromagnetic solution is the slave process since it simply provides 'load' data when needed or requested. Since this relationship between flow and electromagnetics may not hold in other types of simulations, both codes were designed to function as either a master or slave process. At given intervals in the solution sequence the master procedure decides that new data are needed from the slave process. The master then sends any needed fields (e.g. temperature, material state) to the slave and waits for a reply. The slave

computes a new field solution using the new data, sends the requested data (e.g. Joule heating, Lorentz forces) back to the master and waits for another request. The major requirement for such a data exchange type of coupling is the ability to control code (processor)-to-code (processor) data transfers in a continuous and seamless manner. The message-passing utilities developed for parallel processing environments provide such a capability. In the present case the Parallel Virtual Machine (PVM) software[25] was utilized, through other comparable products such as the Message-Passing Interface (MPI)[26] could have been used. The overall data exchange process can be developed to make allowances for the use of different computational meshes for the master and slave solutions. This requires that a mesh-to-mesh translator be inserted between the mechanics codes, but this is still easily accommodated through the PVM software. For time-dependent problems any inherent differences in time scale between the mechanics phenomena can be treated through subcycling of one of the solutions. Though this type of coupling method has great applicability, particularly for VAR applications, it is not without some drawbacks. Most notable is the degraded convergence behaviour for strongly coupled, non-linear physical systems. Full details of the proposed exchange method, its strengths and limitations and its implementation are provided in Reference 11.

4. EXAMPLE SIMULATIONS

The algorithm outlined in the previous sections has been used to study a number of VAR problems involving a uranium–niobium alloy (U–6 wt.% Nb). This alloy was selected because of its strong tendency for macrosegregation and the extensive experimental results that are available[3,27,28] for a variety of processing conditions. Prior to attempting fully coupled simulations of the VAR process, several simpler cases were analysed to verify the flow and electromagnetic solutions and determine appropriate mesh densities.

4.1. Preliminary simulations

The NACHOS II code used in this study has been previously tested on a wide variety of isothermal and non-isothermal flow problems, including benchmark computations.[29,30] Though the basic accuracy of the code has been demonstrated, the question of mesh adequacy and mesh independence always arise for new applications. In the present work a simplified VAR problem was used to test several grid refinements before proceeding with full simulations. An axisymmetric cylindrical region was meshed with three increasingly refined grids of nine-node finite elements. Grids 1, 2 and 3 were defined by mesh densities of 10×40, 20×80 and 20×120. Other more refined grids were tested but produced no further changes in the solution and are not reported here. In each case the upper third of the cylinder contained at least half of the elements, since this region contains all of the melt pool. At low power inputs the mesh was uniform in the radial direction and biased towards the upper surface of the ingot. Higher power inputs required that the mesh also be biased towards the outer surface of the ingot, since the melt pool has a larger radial extent.

The flow problem consisted of a melt pool driven by thermal buoyancy forces only; no Lorentz forces were included in these tests. The melt pool did include the mushy zone as modelled by the Darcy–Brinkman equations for all the relevant material property dependences outlined previously. A set of typical VAR parameters for the U–6 wt.% Nb alloy is given in Table I. Converged solutions for two input heat flux levels were obtained on each grid. The flux levels were selected arbitrarily to produce melt pools of different sizes. The solution procedure used an incrementation and continuation strategy with the Grashof number as a parameter. At each value of the Grashof number, various combinations of Picard and Newton iteration were employed to obtain a solution. A relaxation parameter was sometimes required to assist convergence. Also, the separation point for the

Table I. Material properties and VAR processing parameters for U–6wt.% Nb alloy

Material property	Value	Units
Density	$1{\cdot}56 \times 10^{4}$	kg m^{-3}
Specific heat	200·0	J kg^{-1} K^{-1}
Thermal conductivity	30·0	J m^{-1} s^{-1} K^{-1}
Viscosity	$5{\cdot}0 \times 10^{-3}$	kg m^{-1} s^{-1}
Thermal expansion	$7{\cdot}4 \times 10^{-5}$	K^{-1}
Latent heat	$8{\cdot}0 \times 10^{4}$	J kg^{-1}
Liquidus temperature	1605·5	K
Solidus temperature	1440·0	K
Intrinsic permeability	$1{\cdot}0 \times 10^{-8}$	m^2
Electric conductivity	$1{\cdot}5 \times 10^{6}$	Ω^{-1} m^{-1}
Magnetic permeability	$4\pi \times 10^{-7}$	H m^{-1}
Processing parameter	**Value**	**Units**
Current	6·0	kA
Power	168·0	kW
Efficienty	0·53	
Melt rate	740·0	kg h^{-1}
Ingot radius	0·1042 (4·1)	m (in)
Electrode radius	0·0780 (3·1)	m (in)
Non-dimensional parameter	**Definition**	**Value**
Pr_0	$\mu_0 C_{p_0}/k_0$	0·033
Gr_0	$\rho_0^2 g \beta_0 \Delta T R^3/\mu_0^2$	$1{\cdot}3 \times 10^{9}$
Da_0	κ_0/R^2	$9{\cdot}2 \times 10^{-9}$
Pr_m	$\rho_0 \mu_m \sigma_e/\mu_0$	$6{\cdot}0 \times 10^{-7}$
Ha_0^2	$B_0^2 R^2 \sigma_e/\mu_0$	1723·1
Jo_0	$J_0^2 R^2/\sigma_e/k_0 \Delta T$	$4{\cdot}5 \times 10^{-2}$

ingot was fixed for these cases, which helped improve the iterative convergence. Because Lorentz forces were not included to counterbalance the buoyancy forces, the full value of the Grashof number could not be reached. The grid tests were performed at a Grashof number of $1{\cdot}3 \times 10^{5}$.

Shown in Table II are maximum and minimum nodal point values for several variables obtained on the various grids. The approach to a mesh-independent solution is clear. The differences between meshes 2 and 3 are generally less than 3·5%, except for the derivative (heat flux) values which converge more slowly with mesh refinement. Mesh 2 was adopted for most of the subsequent runs since it showed good accuracy and was somewhat less costly.

The mesh refinement test also provides some insight into the basic flow characteristics to be expected from the VAR simulations. Shown in Plates 1 and 2 are contour plots of the streamfunction and temperature fields for the two heat flux levels. Superimposed on each streamfunction plot is a shaded band that spans the liquidus and solidus contours and defines the extent of the mushy zone. The convective cell rotates clockwise, transferring energy from the incoming metal near the centreline to the edge of the melt pool and subsequently to the boundary of the ingot. The convection at the lower flux values is still relatively weak, since the isotherms are conduction-like in shape. The isotherms for the higher-flux case are clearly altered by the flow and have a more stratified appearance. At the ingot boundary the shape of the isotherms is influenced by the change in boundary condition at the ingot shrinkage (separation) point. Though these solutions show trends in the

Table II. Mesh convergence of flow solution for two power inputs

Low flux level			
	Mesh 1 (10 ×40)	Mesh 2 (20 ×80)	Mesh 3 (20 ×120)
Maximum ψ^*	−4·363 ×10^{-3}	−7·751 ×10^{-3}	−8·576 ×10^{-3}
Maximum u^*	0·2685	0·3676	0·3878
Minimum u^*	−0·1661	−0·2363	−0·2400
Maximum v^*	0·1134	0·1340	0·1381
Minimum v^*	−0·1125	−0·1412	−0·1539
Maximum Θ^*	5·607	5·443	5·388
Maximum q_x^*	2·543	2·572	2·767
Maximum q_y^*	1·473	2·392	2·859
High flux level			
Field variable	Mesh 1 (10 ×40)	Mesh 2 (20 ×80)	Mesh 3 (20 ×120)
Maximum ψ^*	−9·370 ×10^{-2}	−11·920 ×10^{-3}	−11·920 ×10^{-3}
Maximum u^*	1·022	1·340	1·307
Minimum u^*	−1·025	−1·139	−1·125
Maximum v^*	0·673	0·802	0·798
Minimum v^*	−1·261	−1·856	−1·794
Maximum Θ^*	26·48	24·46	24·38
Maximum q_x^*	12·56	13·56	13·52
Maximum q_y^*	6·128	9·824	11·79

simulation, they are not realistic owing to the absence of the Lorentz forces and the unrealistically high temperatures that are predicted on the surface of the melt pool.

The electromagnetic solution algorithm as implemented in the TORO II code was also verified for accuracy before being coupled to the flow problem. Mesh refinement studies like those reported above were carried out for a simplified magnetostatic problem. This problem also has an analytic solution, which simplifies the evaluation of accuracy for the numerical solution. The problem again consists of a cylindrical ingot with the electric current density specified over the top surface. The lateral and bottom surfaces of the region are grounded with a zero electric potential. As reported in Reference 20, the current **J** and magnetic flux **B** can be obtained throughout the region; the spatial distribution of the Joule heating and the components of the Lorentz force then follow directly. The numerical solution to this problem was generated on mesh 2 with constant material properties. Two types of numerical solution were used in the evaluation. In the first case, labelled V, A_r, A_z, the electric potential field within the ingot was computed based on the specified current flux at the boundary. The current densities from this solution were then used as source terms for the magnetostatic field computation. A second solution method, labeled A_r, A_z, used the analytic solution to provide the current densities for the magnetic field; the electric potential was not computed. Shown in Table III are a number of quantities that illustrate the quality of the numerical simulations. Alterations in the mesh density had a relatively small effect on the solution, since this problem is made up of a series of linear diffusion equations that are generally undemanding with respect to mesh refinement.

4.2. VAR simulations

Following the selection of an adequate mesh, several coupled VAR simulations were completed. The problem of interest considered most of the conditions described in the individual flow and

Table III. Comparison of computed electromagnetic field variables with analytic solution

Field variable	Analytic solution	V, A_r, A_z solution	A_r, A_z solution
Maximum V	9·444	9·420	—
Maximum J_r	$1{\cdot}264 \times 10^5$	$1{\cdot}263 \times 10^5$	$1{\cdot}263 \times 10^5$
Maximum J_z	$-2{\cdot}172 \times 10^5$	$-2{\cdot}141 \times 10^5$	$-2{\cdot}197 \times 10^5$
Maximum B_θ	69·06	72·06	72·09
Maximum Q_J	3·039	2·936	2·939
Maximum F_r	921·7	866·2	873·0
Maximum F_z	933·7	895·3	896·1

electromagnetic solutions of the previous section. The ingot material was a U–6 wt.% Nb alloy that was nominally processed at a current of 6 kA and a melt rate of 740 kg hr^{-1}. A series of three computations was completed with the fraction of total current passing through the ingot providing the controlling independent variable for the simulations. Current fractions of 60% (3·60 kA), 71% (4·25 kA) and 85% (5·10 kA) were selected, with all other parameters remaining fixed. The separation point was characterized by a shrink temperature of 800 K. These examples were intended to demonstrate the viability of the method for realistic processing conditions; an in-depth study of processing parameters and comparison with experiment will be developed in a separate report.

The solution strategy for the coupled problem involved a sequence of steady solutions, with various terms in the momentum and energy equations being scaled to provide control of the solution process. Unlike the buoyancy-only test problem of the previous section, the Grashof number was not used directly as an embedding parameter. Rather, the viscous and thermal diffusion terms were multiplied by independent scale factors that started with values of several hundred and were reduced to unity over the course of the solution. The solution strategy was designed to keep the primary forces, Lorentz and buoyancy, in balance as much as possible. To start the solution process, the Hartman and Joule heating numbers were set to zero and all other non-dimensional quantities were set to their full values; the scale factors were set to 'large' values. The heat flux to the surface was adjusted to produce a small melt pool and a reasonable surface temperature. This solution was converged using a combination of Picard and Newton iteration. A series of steps with increasing heat flux and decreasing scale factors led to a larger melt pool. The coupling with the electromagnetic field was then introduced with fixed flow parameters and non-zero Hartman and Joule heating numbers. Convergence at this point again required a combination of Picard and Newton iteration with varying amounts of relaxation. The creation of a second (Lorentz) convection cell was a major change in the solution path and in some cases required more than 20 iterations. When the two-cell solution was established, a series of steps with decreasing scale factors led to the final converged state. During the solution sequence the Lorentz forces and Joule heating were updated periodically through a PVM transfer between the two codes. The most recent temperature field was transferred to the electromagnetic code and a new force and heating distribution were returned to the flow code. In some cases, as the viscosity/conductivity scale factors were reduced, the thermal convection cell would begin to dominate the flow and, if unchecked, would eliminate the Lorentz cell. Reintroduction of a larger Lorentz force (more current through the ingot) at this point in the continuation path would normally lead to divergence of the solution. Increases in the Lorentz force could only be made when both cells were present.

Shown in Plates 3–5 are contour plots of the flow field and temperature field for the three different current inputs to the ingot. The plot scales for the streamfunction and temperature are the same for all three cases so that the changes in magnitude of the two cells can be readily seen. As the electric

current density increases, the clockwise-rotating Lorentz cell strengthens and grows in size. Conversely, the counterclockwise rotation of the thermally driven cell decreases and the cell pair is pushed downwards into the slightly growing melt pool. The temperature field is horizontally stratified within the melt pool for all three current levels. At the highest current the Lorentz cell is sufficiently strong to perturb the stratification at the centreline and create an enlarged region of high-temperature melt. Note that in all three cases the maximum temperature is located off the ingot axis, through the surface temperature within the melt pool is nearly uniform.

The extent of the mushy zone has been indicated in each streamfunction plot. At the highest current level (Plate 5) the streamlines within the mushy zone have been left visible to show the relative magnitude of the flow within this region. The upper half of the mushy layer has a fairly large permeability and a clear effect of the flow can be identified. Lower in the mushy zone the permeability decreases and the fluid motion is slowed considerably. The mushy zone intersects the top surface of the ingot, indicating the presence of a skull or solid shelf next to the crucible; this is consistent with observation.

Shown in Plates 6 and 7 are some of the electromagnetic fields that correspond to the highest current level. Fields for the other two cases are similar in spatial distribution but with reduced magnitudes. The current lines show the obvious effect of having the ingot grounded above the shrinkage and insulated below the separation point. The change in boundary condition at this point leads to singular behaviour in the Joule heating and Lorentz force. This artefact does not influence or complicate the simulation of the melt pool, since separation occurs in the solidified region and the singularity is confined to a heat conduction region.

5. CONCLUSIONS AND COMMENTS

The objective of the present work was the development of a realistic numerical simulation capability for vacuum consumable are remelting problems. The methods outlined here consider most of the major features involved in alloy processing. These include the flow in the melt pool and the mushy zone, heat transfer throughout the ingot and the effects of the electromagnetic environment. The finite element methods used for the non-isothermal flow field and electromagnetics were developed separately and coupled, for the present application, through the PVM software. This has proven to be a flexible and effective method for generating a multiphysics simulation capability.

Though the current method is capable of producing results that correspond at least qualitatively with real processing conditions, the model development is not complete. Of major importance is the inclusion of solute transport and the prediction of macrosegregation. The addition of Marangoni effects and the capability to examine electromagnetic stirring is also viewed as important. A refinement of the thermal portions of the model, including enclosure radiation and a better representation of the arc, would relieve a great deal of the uncertainty present in the heat transfer predictions. The present formulation should be coupled to a solid mechanics solution that would predict the shrinkage point and not rely on an assumed temperature for the determination of separation. Finally, the solution strategy is uncertain and tedious because of its reliance on continuation and the presence of large non-dimensional parameters. Some type of automation or adaptivity would be a welcome development in this area, though this is a long-standing problem in computational fluid dynamics. This uncertain path to a solution certainly needs to be improved if simulation is to be used for routine industrial applications.

ACKNOWLEGEMENTS

This work was performed at Sandia National Laboratories and is supported by the U.S. Department of Energy under contract DE-AC04-94AL85000.

REFERENCES

1. L. A. Bertram and F. J. Zanner, 'Interaction between computational modeling and experiments for vacuum consumable are remelting,' in H. D. Brody and D. Apelian (eds), *Proc. Conf. on Modeling of Casting and Welding*, TMS-AIME, Warrendale, PA, 1980, pp. 333–349.
2. L. A. Bertran and F. J. Zanner, 'Plasma and magnetohydrodynamics problems in vacuum consumable arc remelting', in *Metallurgical Applications of Magnetohydrodynamics*, The Metals Society, London 1982, pp. 283–300.
3. F. J. Zanner and L. A. Bertram, 'Vacuum arc remelting—an overview', *Proc. 8th Int. Conf. on Vacuum Metallurgy*, Vol. 1, 1985, pp. 512–552.
4. A. S. Ballantyne and A. Mitchell, 'Modelling of ingot thermal fields in consumable electrode remelting process', *Ironmaking and Steelmaking*, **4**, 222–239 (1977).
5. A. Jardy, L. Falk and D. Ablitzer, 'Energy exchanges during vacuum arc remelting;, *Ironmaking and Steelmaking*, *19*, 226–232 (1992).
6. P. J. Prescott, F. P. Incropera and W. D. Bennon, 'Modeling of dendritic solidification systems: reassessment of the continuum momentum equation', *Int. J. Heat Mass Transfer*, **34**, 2351–2359 (1991).
7. P. J. Prescott and F. P. Incorpera, 'Numerical simulation of a solidifying Pb–Sn alloy: the effects of cooling rate on thermosolutal convection and macrosegregation', *Metall. Trans. B*, **22**, 529–540 (1991).
8. A. D. Brent, V. R. Voller and J. K. Reid, 'Enthalpy–porosity technique for modeling convection–diffusion phase change: application to melting of a pure metal', *Numer. Heat Transfer*, **13**, 297–318 (1988).
9. V. R. Voller, A. D. Brent and C. Prakash, 'The modeling of heat, mass, and solute transport in solidification systems', *Int. J. Heat Mass Transfer*, **32**, 1719–1731 (1989).
10. C. Beckerman and R. Viskanta, 'Double-diffusive convection during dendritic solidification of a binary mixture', *PhysicoChem. Hydrodyn.*, **10**, 195–213 (1988).
11. D. K. Gartling and S. E. Gianoulakis, 'A data exchange methodology for coupled finite element simulations', in preparation.
12. J. A. Shercliff, *A Textbook of Magnetohydrodynamics*, Pergamon, New York, 1965.
13. D. K. Gartling, C. E. Hickox and R. C. Givler, 'Simulations of coupled viscous and porous flow problems', *Int. J. Comput. Fluid Dyn.*, **7**, 23–48 (1996).
14. J. D. Jackson, *Classical Electrodynamics*, 2nd edn., Wiley, New York, 1975.
15. P. P. Silvester and R. L. Ferrari, *Finite Elements for Electrical Engineers*, Cambridge University Press, Cambridge, 1990.
16. D. K. Gartling, 'Finite element analysis of convective heat transfer problems with change of phase', in K. Morgan, C. Taylor and C. A. Brebbia (eds), *Computer Methods in Fluids*, Pentech, London, 1980, pp. 257–284.
17. C. M. Oldenburg and F. J. Spera, 'Hybrid model for solidification and convection', *Numer. Heat Transfer B*, **21**, 217–229 (1992).
18. D. R. Poirier, 'Permeability for flow of interdendritic liquid in columnar–dendritic alloys', *Metall. Trans. B*, **18**, 245–255 (1987).
19. M. C. Fleming, *Solidification Processing*, McGraw-Hill, New York, 1974.
20. L. A. Bertram, 'A mathematical model for vacuum-consumable-arc remelt casting', *Proc. 1st Int. Conf. on Mathematical Modelling*, 1977, pp. 1173–1183.
21. D. K. Gartling, 'NACHOS II—a finite element computer program for incompressible flow problems', *SAND86-1816*, Sandia National Laboratories, Albuquerque, NM, 1987.
22. J. N. Reddy and D. K. Gartling, *The Finite Element Method in Heat Transfer and Fluid Dynamics*, CRC Press, Boca Raton, FL, 1994.
23. G. F. Carey and J. T. Oden, *Finite Elements, Fluid Mechanics, Vol. VI*, Prentice-Hall, Englewood Cliffs, NJ, 1986.
24. D. K. Gartling, 'TORO II—a finite element computer programe for nonlinear quasi-static problems in electromagnetics', *SAND95-2472*, Sandia National Laboratories, Albuquerque, NM, 1995.
25. A Geist, A. Beguelin, J. Dongarra, W. Jiang, R. Manchek and V. Sunderam, 'PVM 3 user's guide and reference manual', *ORNL/TM-12187*, Oak Ridge National Laboratory, Oak Ridge, TN, 1994.
26. W. Grupp, E. Lusk and A. Skjellum, *Using MPI: Portable Parallel Programming with the Message-Passing Interface*, MIT Press, Cambridge, MA, 1994.
27. F. J. Zanner, 'Metal transfer during vacuum consumable arc remelting', *Metall. Trans. B*, **10**, 133–142 (1979).
28. F. J. Zanner, 'Observations of the vacuum arc and metal transfer during vacuum consumable arc remelting', in G. K. Bhat and R. Schlatter (eds), *Proc. Int. Conf. on Special Melting*, Amermican Vacuum Society, 1979, pp. 417–427.
29. G. de Vahl Davis and I. P. Jones, 'Natural convection in a square cavity: a comparison exercise', *Int. j. numer. methods fluids*, **3**, 227–248 (1983).
30. D. K. Gartling, 'A test problem for outflow boundary conditions—flow over a backward facing step', *Int. j. numer. methods fluids*, **11**, 953–967 (1990).

